Rheological control on earthquake source kinematics and dynamics at the Hengill geothermal field

Vincenzo Convertito[1], Sergio Gammaldi[1], Davide Zaccagnino[2,3], Cataldo Godano[4] and Raffaella De Matteis[5]

[1] Istituto Nazionale di Geofisica e Vulcanologia, Sezione Osservatorio Vesuviano, Napoli, Italy.

[2] Institute of Risk Analysis, Prediction and Management (Risks-X), Academy for Interdisciplinary Studies, Southern University of Science and Technology (SUSTech), Shenzhen, Guangdong, China.

[3] Istituto Nazionale di Geofisica e Vulcanologia, Sezione Roma 1, Roma, Italy.

[4] Department of Mathematics and Physics, Università della Campania-Luigi Vanvitelli, Caserta, Italy.

[5] Dipartimento di Scienze e Tecnologie, Università degli Studi del Sannio, Benevento, Italy.

Corresponding authors: Vincenzo Convertito (vincenzo.convertito@ingv.it); Raffaella De Matteis (raffaella.dematteis@unisannio.it)

Key Points:

- Non-standard scaling of source parameters at Hengill geothermal field
- Difference in static stress drop values between induced and tectonic earthquakes
- Low radiation efficiency suggests positive dynamic overshoot
- Cascade suppression explains positive b-value vs stress drop correlation

Abstract

We analyze seismic source parameters of the induced earthquakes at the Hengill (Iceland) between 2018 and 202 to investigate rupture processes in a complex volcanic–geothermal setting. Our analysis reveals a source scaling relation that deviates from the commonly assumed $M_0 \propto f_c^{-3}$. By combining stress tensor orientation, lithostatic and hydrostatic pressure, and frictional strength estimates, we quantify how much of the available effective stress is released by each earthquake. The results show a consistent depth transition: shallow earthquakes (< 3–4 km) rupture in a fluid–weakened regime, whereas deeper events (> 5 km) are increasingly controlled by ambient tectonic stress. This, combined with low Savage-Wood efficiency indicating significant dynamic overshoot, suggests that a large portion of the available strain energy is dissipated aseismically. To explain these observations, we propose a model where ductile, rate-dependent fracture energy suppresses earthquake cascades. This model successfully predicts the observed null/positive correlation between *b*-value and stress drop, a signature of a high-dissipation regime where increased stress drops suppress rupture propagation rather than promoting it.

Plain Language Summary

Geothermal fields such as Hengill (Iceland) produce both natural and human-triggered earthquakes. Understanding how these earthquakes start and how they release energy is important to reduce risk. We analyzed more than 8600 earthquakes recorded between 2018 and 2021. We estimated how much stress is released by each earthquake and how efficiently they radiate energy. Our results show that shallow earthquakes behave differently from deeper ones. Near the surface, where fluids circulate and geothermal operations take place, earthquakes release proportionally less tectonic stress, likely because fluids weaken the rocks. At larger depths, earthquakes behave more like tectonic events, and stress controls rupture more directly. We also find that only a small fraction of the available energy is radiated as seismic waves. These results suggest that physical conditions change strongly with depth in Hengill, and that induced and natural earthquakes may follow different physical rules in the same area.

1 Introduction

Whether induced earthquakes follow the same physical scaling laws as tectonic earthquakes is still not fully understood. This question is particularly relevant in geothermal fields, where pore-fluid pressure, thermo–hydraulic gradients, and human operations can significantly alter the ambient stress field and the mechanical strength of faults. In these environments, both natural and induced earthquakes can coexist and interact within the same crustal volume, providing a unique opportunity to investigate how rupture properties evolve as a function of depth and fluid conditions.

A clear understanding of the physics of induced earthquakes is key for seismic hazard assessment at geothermal fields (Convertito et al., 2012; Convertito et al., 2021; Douglas et al., 2013). A central controversy in this field concerns the fundamental similarity or difference with tectonic events. This topic has been investigated since early 1990s, when Abercrombie and Leary (1993) first observed a difference in the average stress drop value of induced and tectonic earthquakes. Subsequent research works, such as Huang et al. (2017), have shown that induced and tectonic earthquakes recorded in central United States have similar stress drop values. After more than three decades, the debate is still ongoing. Here, we contribute by analyzing the source parameters of earthquakes recorded in the Hengill (henceforth HG) geothermal field, southwest Iceland, between December 1, 2018, and January 31, 2021 (Figure 1). The HG geothermal area lies on the boundary between the North American and Eurasian plates, and geothermal energy exploitation has been ongoing there since the late 1960s for both electricity generation and district heating. The two largest geothermal power plants in Iceland — Nesjavellir and Hellisheidi — are located within this region, with a total of 76 wells reaching depths of up to 2 km. According to Grigoli et al. (2022), the recorded seismicity in this area includes both induced and natural earthquakes, which makes the Hengill field an ideal site for investigating potential differences between these two types of seismicity.

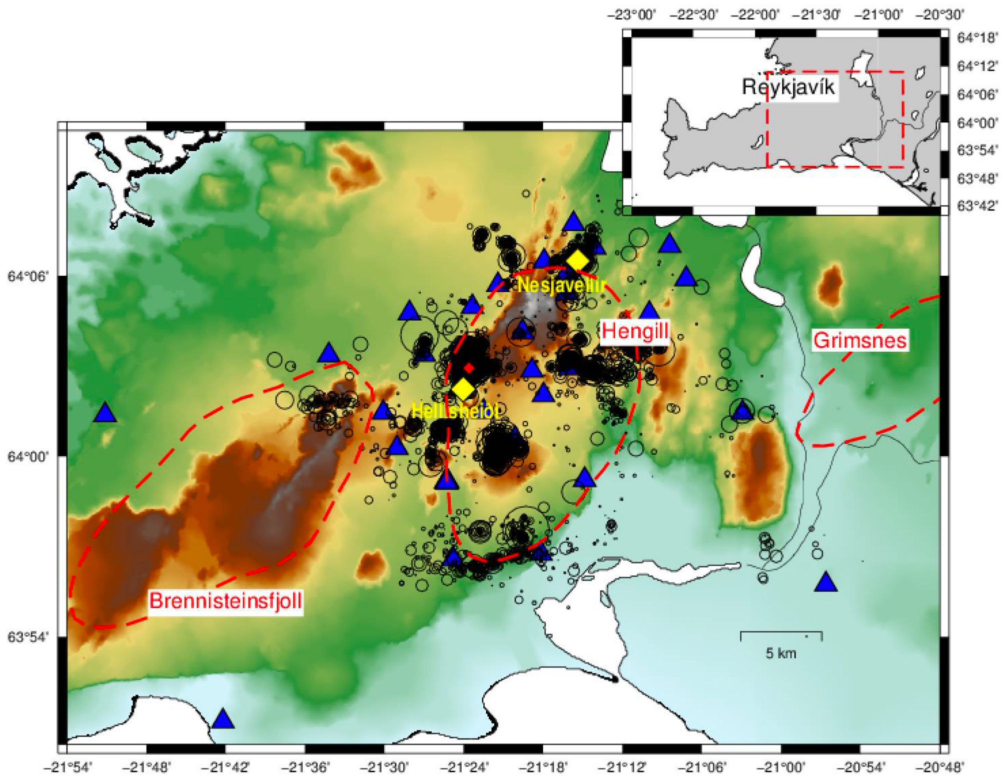

Figure 1. Geographic map of the study region. The map reports the volcanic centers in SW-Iceland (enclosed in red dashed lines), including Hengill, Brennisteinsfjoll and Grimsnes. Yellow diamonds

indicate the two largest geothermal fields, namely, Hellishiði and Nesjavellir. The back circles identify the epicenter of the events analyzed in the present study. The blue triangles represent the stations installed during the COSEISMIQ project (Grigoli et al., 2022). The upper right inset depicts south Iceland region.

While earthquakes recorded in the area have been extensively used to investigate crustal structures through the application of seismic and attenuation tomography (Amoroso et al., 2022; Obermann et al., 2022; Wu et al., 2024; Napolitano et al., 2025), to our knowledge, no previous study has been devoted to study seismic source parameters. Following the approach proposed by Convertito and De Matteis (2025), we estimate kinematic and dynamic source parameters by implementing the individual spectral analysis and an Empirical Green's Function (EGF) approach (Abercrombie, 2015; Ide et al., 2003; Prieto et al., 2006). EGF allows to reduce the problem of the trade-off between source parameters, anelastic attenuation and site-effect while fitting the recorded spectrum. We analyze the scaling between corner frequency and seismic moment and between radiated energy and seismic moment that allowed us to infer seismic efficiency. We also investigate the depth dependence of the static stress drop and correlate it with the *b*-value of the Gutenberg-Richter law.

2 Data description

The seismic dataset analyzed in this study was collected in the Hengill geothermal area, southwest Iceland, where several dense monitoring networks operate. The area is continuously monitored by eight permanent seismic stations operated by the Icelandic Meteorological Office (IMO) and ten permanent stations belonging to a microseismic network managed by the Iceland GeoSurvey (ÍSOR) on behalf of Reykjavik Energy. In the framework of the *COntrol SEISmicity and Manage Induced earthQuakes* (COSEISMIQ) project, the monitoring capabilities were further enhanced between October 2018 and August 2021 with the installation of the 2C network, consisting of 23 broadband stations deployed for advanced seismic monitoring purposes (Grigoli et al., 2022). The aperture and spacing of the entire backbone network are ~40 and ~3 km, respectively. The stations are equipped with 3-component short-period (5s and 1s) and broadband (120s and 60s) sensors with sampling rates of 100 and 200 sps. The available catalogue counts 8691 events whose magnitude M_L ranges between −0.78 and 4.56. As described by Grigoli et al. (2022) the real-time management techniques implemented in the project allow to provide both continuous waveforms and double difference earthquakes' locations, those latter indicating that the depth of the events ranges between 0.0 and 14.3 km.

We correct the recorded velocity waveforms for instrument response and filter them in the range (0.5, 80.0) Hz by applying a band-pass filter. To select P- and S-wave signals for each event we perform automatic phase picking using the PickNet model (Wang et al., 2019). This model was updated and retrained using the INSTANCE (Michelini et al., 2021), STEAD (Mousavi et al., 2019), and DiTing (Zhao et al., 2023) phase-picking datasets recently used for tomography purposes in volcanic area (Gammaldi et al., 2025). The initial set of phase picks was filtered based on quality. We converted the pick probabilities into integer quality weights ranging from 0 to 4, and we discarded any pick with a weight greater than 1 (corresponding to a probability below 0.75). We use the high-quality picks to estimate the V_P/V_S-ratio for each event using simil-Wadati method.

3 Methods and analyses

In the present study, we implement the procedure described in Convertito and De Matteis (2025), whose main points are summarized here for the sake of completeness. It is a multistep procedure consisting of:

1. Compute preliminary values of seismic moment, corner frequency and quality factor parameter *Q* for the earthquakes with magnitude greater than 1.9 (e.g., main events) using the individual earthquake spectral analysis.

2. Apply the EGF technique either to refine the estimation of the source parameters of the main events and to infer source parameters of the events used as EGFs.

3. Estimate the Q-factor from the individual earthquake spectral analysis for the main events by setting the seismic moment and corner frequency to the values obtained in the previous analysis (point 2).

4. Compute the radiated energy from the observed source spectra corrected by the anelastic attenuation.

3.1 Individual earthquake spectral analysis

Spectral analysis and source parameters estimation require to account for all those factors that modify the signal originated at the source and recorded on the earth surface: source radiation, wave propagation, and near-site effects. The general formulation of the displacement spectrum together with the anelastic attenuation filter is given by:

$$S(f) = \frac{\Omega_o}{\left[1+\left(\frac{f}{f_c}\right)^{\gamma n}\right]^{\frac{1}{\gamma}}} e^{-\frac{\pi f T}{Q}} \qquad (1)$$

Where Ω_o is the spectral level at low-frequency that allows to obtain the earthquake seismic moment, f_c is the corner frequency, which is related to the fault dimension, and n is the high-frequency falloff.

The constant γ controls the shape of the corner and T is the travel time of the selected phase. The Brune (1970) source model corresponds to using $n = 2$ and $\gamma = 1$, while for the Boatwright (1980) source model $n = 2$ and $\gamma = 2$.

We analyze 17 earthquakes with local magnitude $M_L > 1.9$, recorded by those stations sampled at 200 Hz to ensure a broad frequency bandwidth. For the P-wave, we extracted a 1.5 s window (0.5 s before and 1.0 s after the P-pick) from the vertical component. The signal was cosine-tapered and zero-padded before computing the displacement spectrum using the multi-taper method (Prieto et al., 2007). Given the source-to-station distance range, the selected window avoids S-wave contamination. For the S-wave, a 1.7 s window (0.2 s before and 1.5 s after the S-pick) was applied, and the vector sum of the spectra from the two horizontal components was calculated.

To ensure high quality data selection, for both P- and S-wave, we measure the signal-to-noise ratio (SNR) on the pre-P noise and discard the spectra characterized by a mean value of the log(SNR) lower than 3.0 and for which the percentage of spectral points having log(SNR)<0 is higher than 10%.

The inversion procedure scheme reproduces that adopted by Convertito and De Matteis (2025), which consists of a two-step approach to infer Ω_o, f_c and Q from the observed spectra. The first step is devoted to obtaining a preliminary estimate of Ω_o by analyzing the flat portion – up to 5 Hz – of the displacement spectrum. The selected spectrum is fitted with a zero-slope line to infer Ω_o and its uncertainty σ_{Ω_o}. Next, we allow Ω_o to vary in the range $\Omega_o \pm 3 \cdot \sigma_{\Omega_o}$ and search for f_c adopting a grid search approach.

As reported above we select only the waveforms sampled at 200 Hz for which the effective bandwidth was restricted to 80% of the Nyquist frequency. To minimize the influence of low signal-to-noise ratios, the maximum frequency employed in the spectral inversion was limited to 60 Hz.

Concerning the range of exploration of the model parameters, the upper bound of the f_c search range is set to 40 Hz, consistent with the prescription given by Abercrombie (2015), while for Q we explored (50, 300) both for P- and S-waves. The inferred estimates of Ω_o and f_c are then refined in the EGF analysis.

To select the best parameters, we search for the minimum of the squared difference between the log of the observed spectrum weighted by the SNR at each specific frequency and the log of the theoretical spectrum. We report in Figure 2 waveforms, spectra and spectral fitting for a selected earthquake together with inferred parameters.

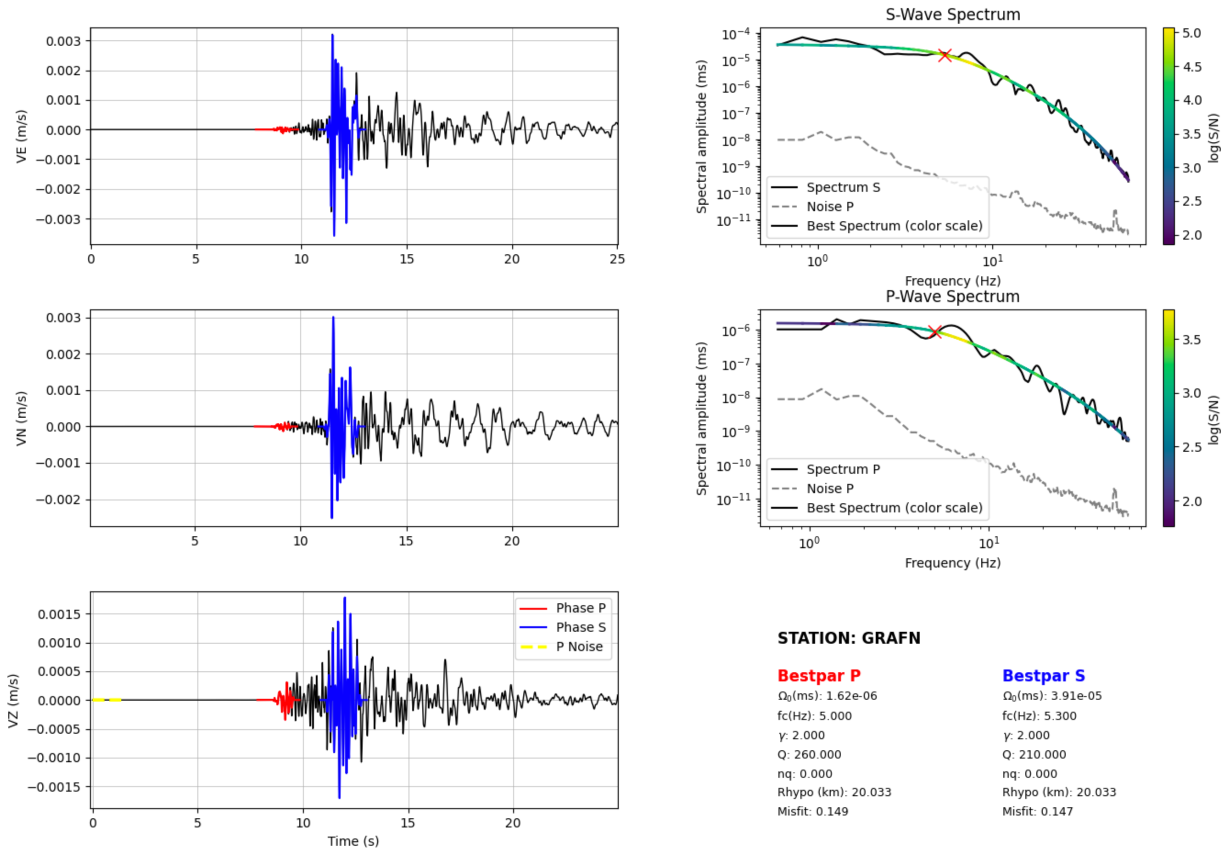

Figure 2. Example of waveform and spectral fitting. The left panels show the three-component velocity seismograms (VE, VN, VZ) filtered in the band (0.1, 90.0) Hz with P- and S-wave selected signal windows (red and blue, respectively) and the P-wave noise window (yellow). The right panels display the corresponding S- (top) and P-wave (bottom) amplitude spectra (black lines) together with the noise spectra (gray dashed lines) and the best spectral fit (colored line). The color scale represents the logarithm of the signal-to-noise ratio [log(S/N)], and the red cross indicates the estimated corner frequency (f_c) from the best spectral fit. The table summarizes the best-fitting source parameters for the P and S phases, including low frequency spectral level $\boldsymbol{\Omega_o}$, corner frequency (f_c), spectral decay parameter (γ), quality factor (Q), hypocentral distance (R_{hypo}), and misfit. The nq parameter is the exponent generally adopted in the frequency dependent model $Q(f)=Qf^{\,nq}$ that is set to zero in the present study.

Once Ω_o has been estimated, we compute seismic moment by using crustal model parameters as it follows (e.g., Zollo et al., 2014):

$$M_o = \frac{4\pi \rho_h^{1/2} \rho_o^{1/2} c_h^{5/2} c_o^{1/2} R' \Omega_o}{R_{\theta\varphi}^{c} F_s} \quad (2)$$

Where ρ and c refer to the rock density and velocity (for P- and S-waves), respectively. Subscripts h and o refer to the hypocenter and receiver, respectively. $R_{\theta\varphi}^{c}$ represents the average value of the radiation pattern coefficient, here assumed equal to 0.52 for P-wave and 0.63 for S-wave (Boore and Boatwright, 1984), and F_S is the free-surface coefficient assumed equal to 2. We implemented the formulation proposed by Ben-Menahem and Singh (1981) for the geometrical spreading R' that is calculated assuming a linear variation of the velocity with depth. For each station and for each earthquake, we used the velocity model provided by Grigoli et al. (2022) to compute the take-off angle. The results are shown in Figures 3a and 3b for both P- and S-wave.

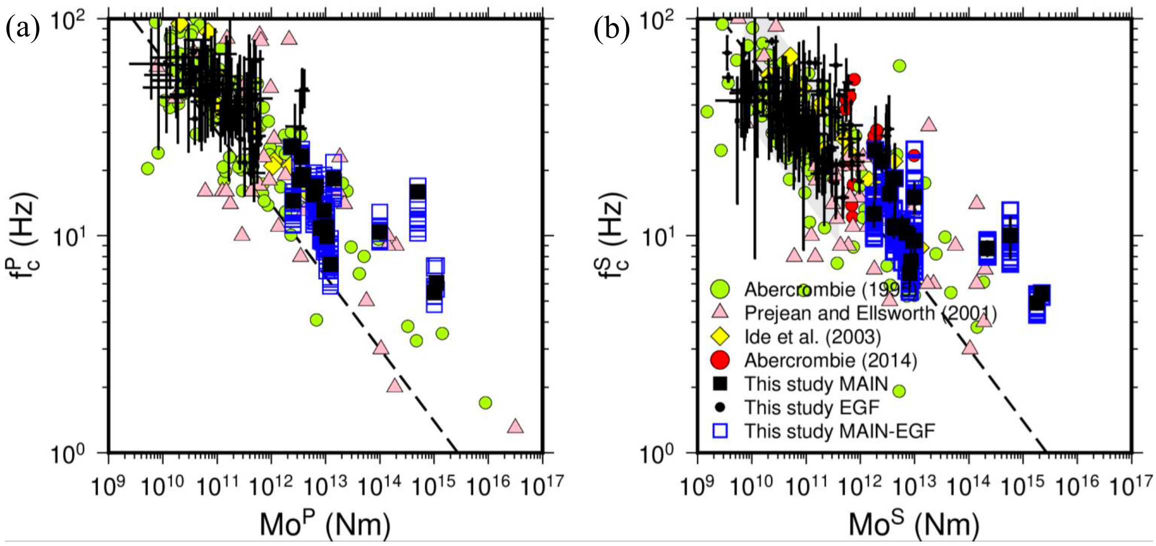

Figure 3. Corner frequency versus seismic moment for the P-wave (panel a) and for the S-wave (panel b). Black squares identify the results obtained from the single-earthquake approach whereas the blue squares depict the results of the spectral ratio analysis for each considered main-EGF couple. In both panels black crosses represent the results for the EGFs. Dashed line indicates the scaling relation $\boldsymbol{M_o} \propto \boldsymbol{f_c^{-3}}$ obtained by using a stress drop of 1 MPa. The green dots, yellow diamonds, and pink triangles correspond to the results obtained by Abercrombie (1995), Ide et al. (2003), and Prejean and Ellsworth (2001), respectively. Red dots in panel b correspond to the values provided by Abercrombie (2014).

3.2 The empirical Green's function (EGF) method

To refine the estimation of the corner frequency and seismic moment of the main events and to infer the source parameters for the smaller earthquakes we implemented the EGF method (e.g., Abercrombie, 2015; Prieto et al., 2006) which, under specific hypotheses, allows to neglect the effect of the anelastic attenuation as well as the site effects for main-EGF pair closely located.

We considered all events with $M > 0$ located at a maximum distance of 1km from the 17 events analyzed with the individual earthquake approach and have a difference in magnitude larger than 1, which resulted in a total of 473 couples.

We consider both P- and S-waves by using the same time window lengths used in the individual spectral analysis. The spectra are computed by using the multi-taper method (Prieto et al., 2007) and their ratio is modeled according to the following equation:

$$\frac{M_1(f)}{M_2(f)} = \frac{M_{o1}}{M_{o2}}\left[\frac{1+\left({f}/{f_{c1}}\right)^{\gamma n}}{1+\left({f}/{f_{c2}}\right)^{\gamma n}}\right]^{\frac{1}{\gamma}} \qquad (3)$$

where f_{c1} and f_{c2} correspond to the corner frequency of the main event and EGF, respectively, and M_{o1} and M_{o2} indicate their seismic moment. Like the analysis of the individual earthquake here we use the Boatwright (1980) source model. We fit each spectral ratio by using a grid-search approach that explores f_{c1} in the range $f_{c_main} \pm 0.6 \cdot f_{c_main}$, f_{c_main} being the value obtained from the individual earthquake analysis, whereas f_{c2} is constrained to be larger than f_{c1} and explored up to 80 Hz. Note that the upper limit of the exploration is higher than that used in the individual event analysis due to the expected higher corner frequency for smaller earthquakes. Finally, the availability of M_{o1} allows to compute M_{o2} and to refine also M_{o1}. We only consider those couples for which the source parameters can be estimated at a minimum of 5 stations and have waveforms' correlation larger than 0.7 to ensure a similar radiation pattern.

Figure 4 shows the waveforms, the spectral ratio and the relative source time function (STF) of the mainshock for a couple main-EGF. The relative STFs have been obtained by implementing the deconvolution technique proposed by Prieto et al. (2007).

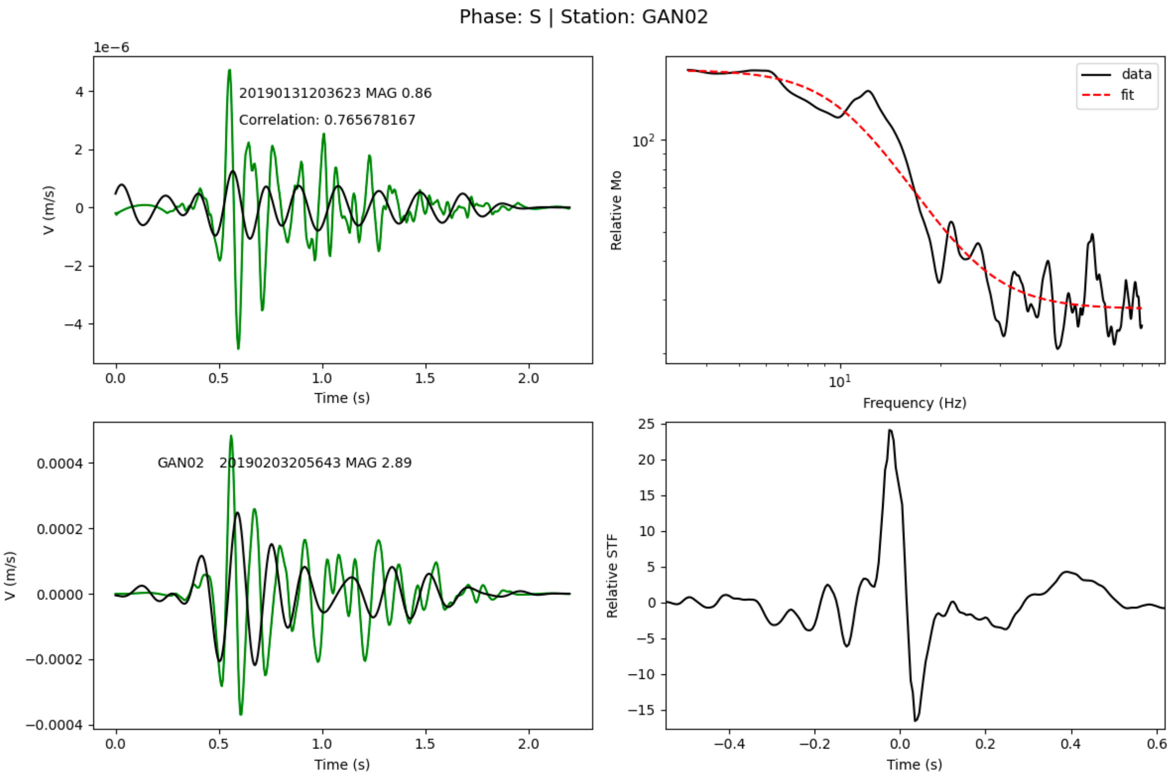

Figure 4. Example of the EGF technique. The left panels show the waveforms of both the main event (bottom) and the EGF (top) filtered in the band (0.1, 90.0) Hz (green curves) and the waveforms filtered in the band (3, 7) Hz used to compute the correlation (black curves). The upper-right panel shows the comparison between the computed spectral ratio (black curve) and the fitting model (red dashed curve) whereas the lower-right panel shows the obtained relative source function.

4 Results

The results shown in Figure 3 suggest a linear scaling for the whole analyzed seismic moment range (10^9 – 10^{15} Nm) that, however, differs from the self-similar scaling $M_o \propto f_c^{-3}$. To quantify the difference, we perform a linear fit of the relation $M_o \propto f_c^{-(3+\varepsilon)}$ that resulted in $\varepsilon = 0.6$ for the P-wave and $\varepsilon = 0.7$ for the S-wave. We compute the stress drop by using the following equation:

$$\Delta\sigma = \frac{7}{16}\frac{M_o}{r^3} = \frac{7M_o}{16}\frac{f_c^3}{k^3\beta^3} \qquad (4)$$

We assume the Brune (1970) source model for the relation between source radius, r, and corner frequency. In equation (4), the symbol β corresponds to the S-wave velocity and $k = 0.37$. The resulting average static stress drop obtained by considering both P- and S-waves is $\Delta\sigma = 6.5 \pm 13.2$ MPa. Figure 5a shows the statics stress drop versus seismic moment, along with results obtained by other authors. We list in Table S1 the retrieved values of the seismic source parameters for the main events and the EGFs. In Figure 6, we show the static stress drop values as a function of depth. A clear increase of $\Delta\sigma$ with depth can be observed, which is further highlighted by the average values computed over three distinct depth ranges corresponding to the locations of the hypocenters. From the same figure it can be noted that in correspondence of the observed increase of the stress drop with the depth there is a slight decrease in the V_P/Vs ratios. These latter have been obtained in the present study from the simil Wadati diagram and are consistent (for the common depth values) with the values obtained by Amoroso et al. (2022) from the seismic tomography performed in the same area.

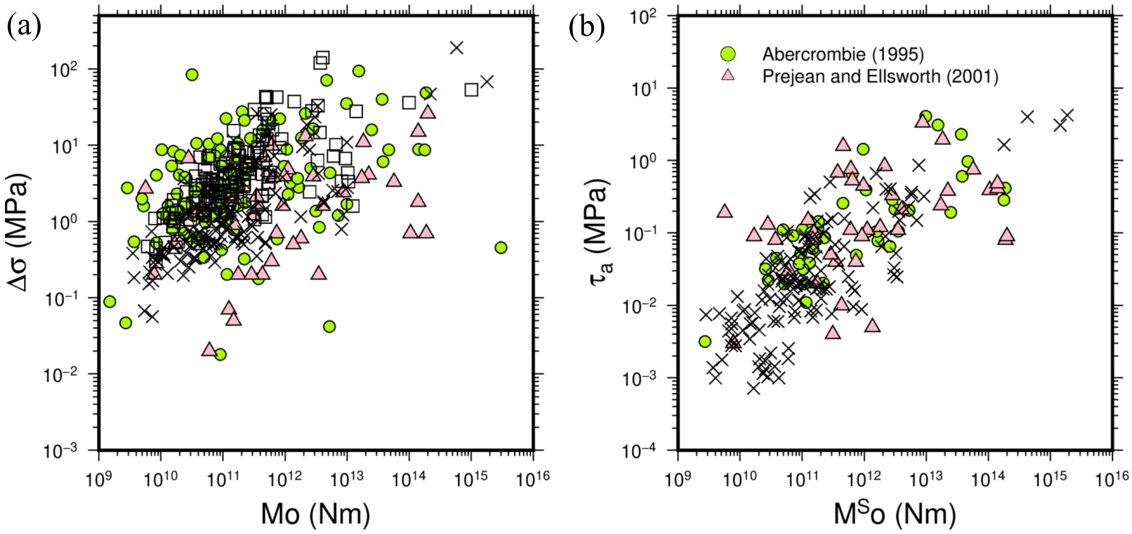

Figure 5: Panel a: the static stress drop as a function the seismic moment for both P-wave (black squares) and S-waves (black crosses). Panel b: apparent stress (black crosses) as a function of the seismic moment for the S-wave. The green dots and pink triangles correspond to the results obtained by Abercrombie (1995) and Prejean and Ellsworth (2001), respectively.

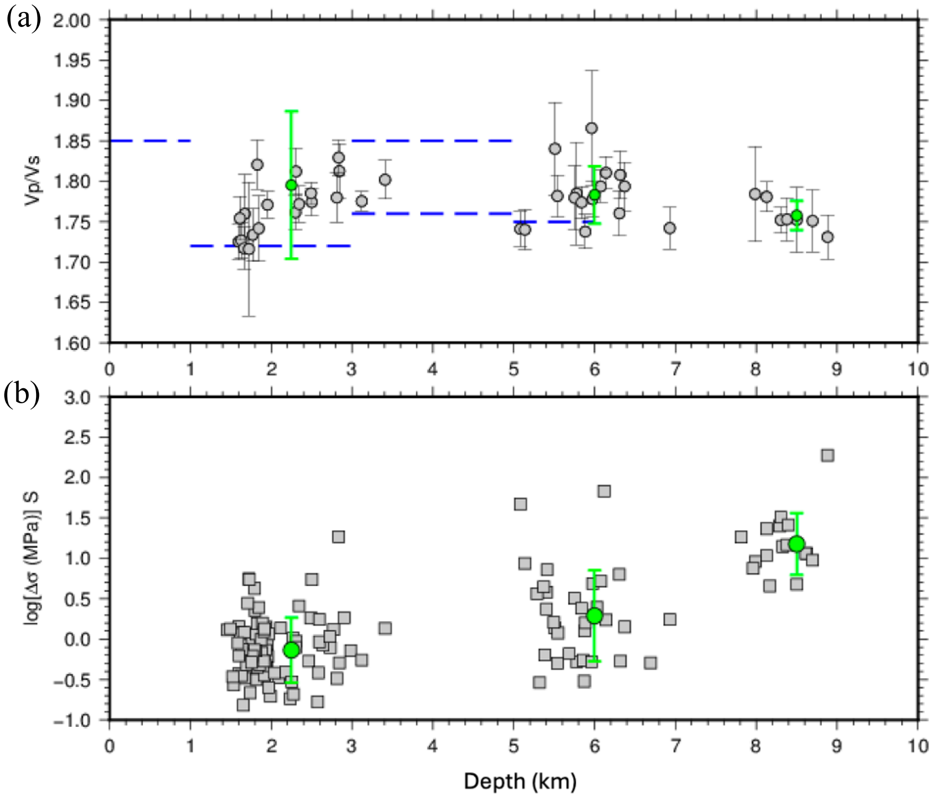

Figure 6: V_P/V_S and static stress drop for the S-wave as function of the earthquakes' depth. V_P/V_S ratio as obtained from the simil Wadati diagram (a) and static stress drop in log scale (b). The green circles represent the average value with the associated error (vertical bar). The horizontal dashed blue lines in panel (a) represent the V_P/V_S values obtained by Amoroso et al. (2022). The two dashed lines for the range 3-5 km indicate the lateral variability observed at those depths in V_P/V_S tomographic model.

Another fundamental parameter for understanding the physics of earthquakes, derivable from the recorded waveforms, is the seismic energy (E) released during the rupture process. In the present study we used the approach proposed by Boatwright et al., (2002) to estimate E from the integral of the squared velocity spectrum, after the correction for anelastic attenuation:

$$E = \frac{4\rho\beta R^2}{F_S^2}\int_0^\infty |\dot{u}(\omega)|^2 e^{\frac{\omega R}{\beta Q}}\, d\omega \qquad (5)$$

In equation (5) $\dot{u}(\omega)$ is the observed velocity spectrum and the other parameters have been described above. Following the approach proposed by Convertito and De Matteis (2025), we estimated the quality factor Q to be used in equation (5) from the individual spectral analysis of the main events. To overcome the trade-off between Q and the source parameters we repeat the analysis for the main events (using the same time windows and frequency range) by setting their seismic moment and corner frequency to the values obtained from the EGF analysis and searching only for the quality factor Q. The obtained results suggest a depth dependence of the Q values. We obtain Q_P =101±24 and Q_S = 142±24 for earthquakes shallower than 5 km while Q_P =156±18 and Q_S = 222±33 for events deeper than 5 km.

The integral in equation (5) is performed up to an upper frequency bound of 60 Hz and the result is further corrected for the frequency band limitation (Ide and Beroza, 2001) by considering the Boatwright source model and the corner frequency estimated at each station. The obtained values for both P- and S-waves are shown in Figure 7 suggesting an overall agreement with those reported by Abercrombie (1995), Ide et al. (2003), and Prejean and Ellsworth (2001). However, particularly for the P-wave, we note an underestimation of the energy at small seismic moments likely due to the narrow available frequency band or to underestimated Q.

By using the estimated seismic energy for the S-wave we also computed the apparent stress $\tau_a = \mu E / M_o$(Wyss, 1979) (using a shear modulus μ= 3.3x10^{10} Pa) and the Savage-Wood seismic efficiency $\eta_{SW} = \tau_a / \Delta\sigma$ (Beeler et al., 2003), which is proportional to the radiation efficiency (Husseini and Randall, 1976).

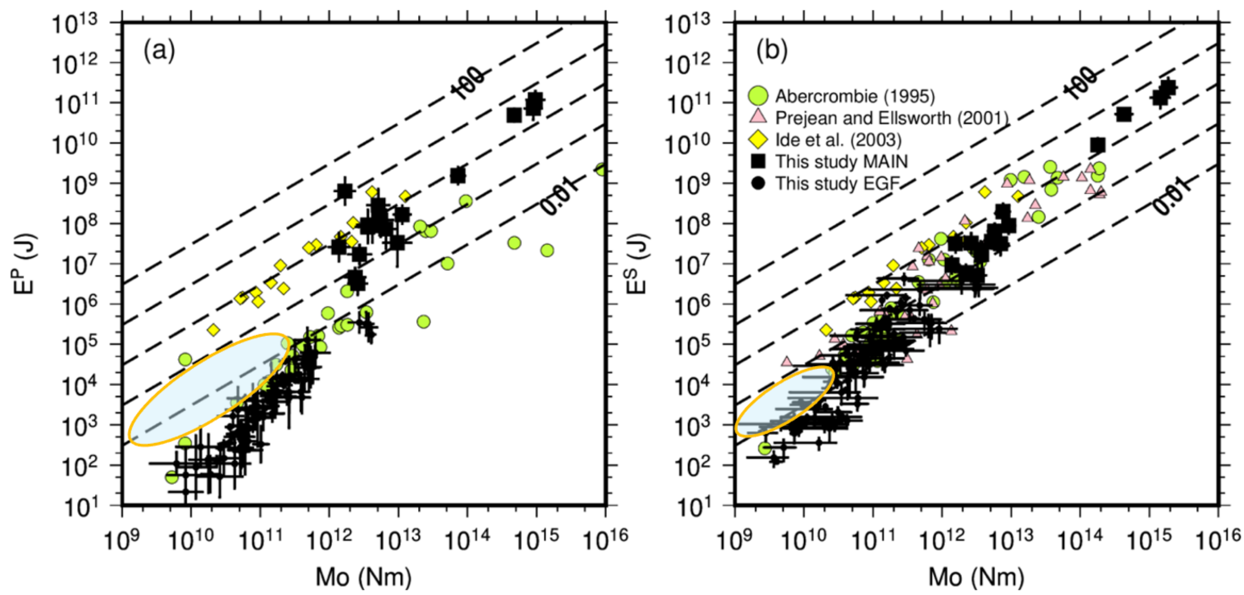

Figure 7: Seismic energy E (black squares) as function of the seismic moment for P-wave (E^P) (a) and for S-wave (E^S) (b). The dashed lines refer to constat apparent stress values in MPa. The green dots, yellow diamonds, and pink triangles correspond to the results obtained by Abercrombie (1995), Ide et al. (2003), and Prejean and Ellsworth (2001), respectively. The ellipse in both panels indicates the energy shortage if a constant linear scaling is assumed.

We report the resulting apparent stress values as function of the seismic moment in Figure 5b while the seismic efficiency values as function of the seismic moment are reported in Figure 8. The average apparent stress is 0.12 ±0.57 MPa whereas the average seismic efficiency η_{SW} is 0.052 ±0.1248, which suggests the occurrence of dynamic overshoot: the final static stress is lower than the final dynamic stress likely due to inertia (e.g., Abercrombie and Rice, 2005; Kanamori and Rivera, 2004). Static stress drops and apparent stress allow us to compute the dynamic stress drop that, assuming that radiated energy is expressed as $E_R = (2\Delta\sigma_d - \Delta\sigma)Mo/2\mu$, is given by $\Delta\sigma_d = \tau_a + \Delta\sigma/2$ (Kanamori and Heaton, 2000). Using the results obtained in the present study for the mean value of the static stress drop ($\Delta\sigma$ = 6.5 MPa) and apparent stress (τ_a = 0.12 MPa), we obtain $\Delta\sigma_d$ = 3.37 MPa, that is, the dynamic stress drop or the effective tectonic stress (Brune, 1970) is about 52% smaller than the static stress drop suggesting a significant dynamic overshoot during the earthquake rupture process.

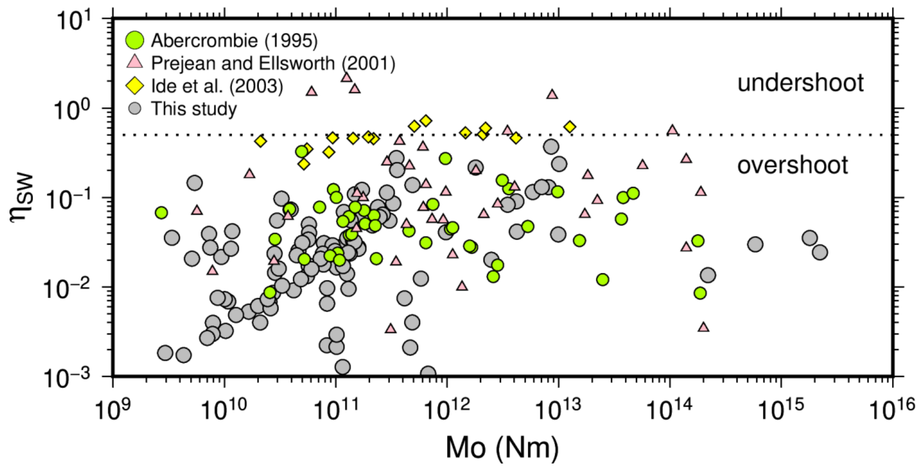

Figure 8. Savage-Wood efficiency as function of the seismic moment (grey circles). The horizontal dotted line indicates the 0.5 threshold, which limits the undershoot from overshoot dynamic weakening mechanisms. The green dots, yellow diamonds, and pink triangle correspond to the results obtained by Abercrombie (1995), Ide et al. (2003), and Prejean and Ellsworth (2001), respectively.

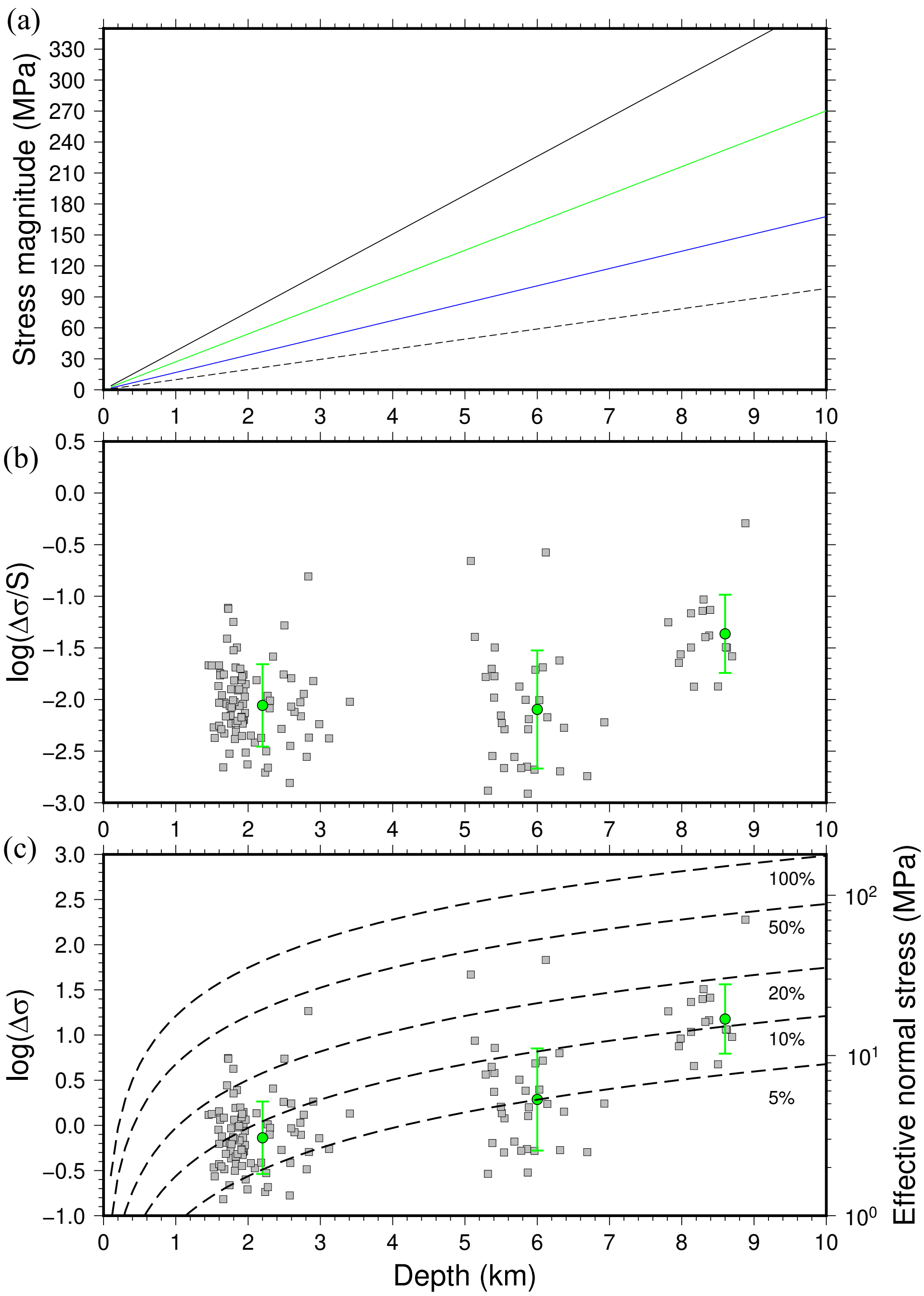

Figure 9. (a) Depth variation of the principal stress magnitudes σ_1 (black), σ_2 (green), and σ_3 (blue), and hydrostatic pressure (black dashed) in the Hengill area. (b) Ratio between static stress drop ($\Delta\sigma$) and shear strength $S = (\sigma_1 - \sigma_3)/2$ as a function of depth. Green dots represent the mean log($\Delta\sigma$/S) value within each of the three selected depth intervals, with the corresponding standard deviation. (c) Percentage of effective normal stress (difference between lithostatic and hydrostatic pressure) released as static stress drop. This comparison highlights systematic differences between shallow and deeper events in terms of stress conditions and stress release efficiency. Green dots represent the

mean log(Δσ) value within each of the three selected depth intervals, with the corresponding standard deviation.

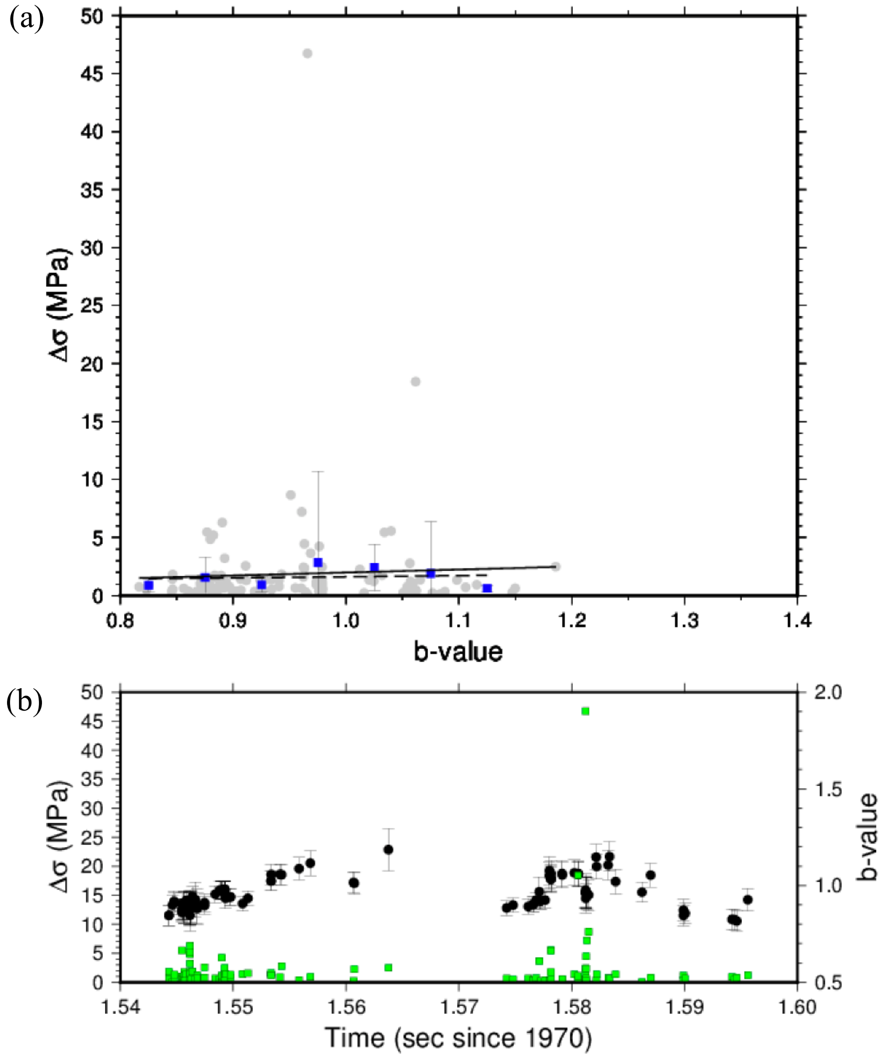

Figure 10. Correlation analysis between b-value and static stress drop. (a) Linear fitting of static stress drop values versus *b*-values. Black continuous line represents the linear best fit on the whole dataset (grey dots) whereas dashed line the linear best fit on binned *b*-value data (blue squares) with associated uncertainty. (b) Black dots represent the *b*-value together with the associated uncertainty whereas green squares represent the log of the static stress drop both plotted as function of time.

5 Discussion

The scaling relations obtained for the Hengill geothermal area in Iceland offer new insights into the source characteristics of earthquakes in a complex volcanic–geothermal environment. The observed seismic moment–corner frequency relationship departs from the trend predicted by self-similar models (e.g., Abercrombie, 1995), following instead the scaling $\mathrm{M_o} \propto f_c^{-(3+\varepsilon)}$.

For the analyzed seismicity we found that $\varepsilon \sim 0.6$ for the P-waves and $\varepsilon \sim 0.7$ for the S-waves. These deviations likely reflect the combined influence of variable stress drop, the role of pore-fluid pressure in earthquake triggering, and the presence of local structural heterogeneity associated with geothermal activity. In the Brune (1970) framework, where $\mathbf{M_0} \propto \Delta\boldsymbol{\sigma} \boldsymbol{f_c^{-3}}$ for circular cracks, the observed steepening of the seismic moment versus corner frequency relation implies that $\Delta\boldsymbol{\sigma} \propto \boldsymbol{f_c^{(3+\varepsilon)}}$ and hence a size-dependent stress drop, $\Delta\boldsymbol{\sigma} \propto \boldsymbol{M_0^{\frac{\varepsilon}{3+\varepsilon}}}$. The observed non-self-similar behavior suggests that rupture processes in the Hengill geothermal field are influenced by scale-dependent variations in strength and stress, consistent with previous findings from other geothermal and volcanic systems (e.g., Goertz-Allmann & Wiemer, 2013; Kwiatek et al., 2011; Convertito & De Matteis, 20025). Shallow events—more affected by strong velocity contrasts and active hydrothermal circulation—are expected to show the largest deviations from ideal scaling, consistent with the enhanced scatter at small magnitudes observed in our dataset.

Looking at the results shown in Figure 6, we found a depth dependence of the static stress drop in particular for events deeper than 6 km. Although it has been argued that such a dependence may arise from the fact that a single constant S-wave velocity is used when computing source radius and thus stress drop (Huang et al., 2017), this is not our case since we select for each earthquake the S-wave velocity corresponding to its depth from the 1D velocity model proposed by Grigoli et al. (2022). Therefore, the increase of the static stress drop is likely caused by the expected increase of the effective normal stress. Moreover, since the maximum depth reached by the injection wells in the area is less than 2 km, deeper events are likely tectonic earthquakes. The results therefore suggest that, at Hengill induced and tectonic earthquakes have different stress drops.

Using the stress tensor orientations provided by Hensch et al. (2016) (σ_1: trend = 32°, plunge = 10°; σ_2: trend = 212°, plunge = 80°; σ_3: trend = 122°, plunge = 5°) in our study area, and a shape factor R = 0.51, we computed the σ_1, σ_2, and σ_3 stress magnitudes and their depth gradients (Figure 10a) following the approach proposed by De Matteis et al. (2024) and Convertito and De Matteis (2025). We adopt a friction coefficient $\mu = 0.75$ and an average density $\rho = 2800$ kg/m^3 (Decriem et al., 2010; Hensch et al., 2016). We also computed the stress magnitudes at the hypocenters of the earthquakes for which static stress drop ($\Delta\sigma$) estimates are available. Assuming that crustal shear strength is expressed as $S = (\sigma_1 - \sigma_3) / 2$, we calculated the ratio between $\Delta\sigma$ and S for each event (Figure 10b), and the percentage of effective normal stress (i.e., the difference between lithostatic pressure $\sigma_v = \rho g z$ and hydrostatic pressure) that is released as static stress drop (Figure 10c). Both the $\Delta\sigma/S$ ratio and the percentage of effective normal stress released differ systematically between shallow and deeper earthquakes. If $\Delta\sigma$ and S increase proportionally with depth, the ratio should remain constant, indicating that the same triggering mechanism and energy release process operate at all depths. Instead, our results (Figure 10) show that this is not the case. Overall, these observations suggest that shallow earthquakes in Hengill nucleate and propagate in a fluid–weakened regime, whereas deeper events are more controlled by ambient tectonic stress. In other words, the physical mechanism controlling rupture and energy release appears to shift with depth.

A similar distinction between shallow and deep earthquakes is observed for the anelastic attenuation factor Q and also, but less markedly, for the V_P/V_S-ratio. We found that both Q_P and Q_S increase with depth. Specifically, Q_P =101±24 and Q_S = 142±24 for the earthquakes shallower than 5 km while Q_P =156±18 and Q_S = 222±33 for the events deeper than 5 km. The resulting Q_S/Q_P-ratio ranges between 1.4 and 1.42 indicating the contribution of pore fluids to the anelastic attenuation of both P-and S-waves. Q_P values smaller than Q_S have been observed from laboratory experiments by Toksoz et al. (1979) for partially fluid-saturated rocks. The presence of fluids and the thermal gradient have been used to explain the variability of the V_P/Vs ratio observed in the tomographic models (Amoroso et al., 2022; Obermann et al., 2022).

We also found that the scaled energy does not increase linearly with seismic moment but follows the relation $\boldsymbol{E/Mo \propto M_0^{0.59\pm0.04}}$, which is consistent with the observed non-self-similar scaling between seismic moment and corner frequency (Kanamori and Rivera, 2004). The departure is likely due to a difference in the static stress drop and rupture velocity among the earthquakes (Kanamori and Rivera, 2004).

The obtained value of the Savage and Wood efficiency $\boldsymbol{\eta_{SW}}$ is equal to 0.1(0.05,0.2), suggesting the occurrence of dynamic overshoot (e.g., Abercrombie and Rice, 2005), which is generally ascribed to inertia, propagation and arrest of expanding cracks (Beleer, 2006). A low radiation efficiency value has been interpreted as the fact that the radiated energy is very small with respect to total available budget of energy. Most of the available energy could be spent by dissipation mechanisms, such as, friction, creation of new fracture surface, permanent deformation, and fluid migration. The same conclusion is obtained from the analysis of the dynamic stress drop.

To further investigate the differences outlined above, we consider an additional parameter: the *b*-value of the Gutenberg–Richter relationship, which characterizes the relative occurrence of small versus large earthquakes within the analyzed dataset. In tectonic areas the *b*-value is close to 1 while it can assume larger value in volcanic areas (e.g., Wiemer et al., 1998; Convertito et al., 2025). It has been shown that the *b*-value increases with the degree of heterogeneity of the crust (Mogi et al.,1962) and temperature gradient (Wiemer et al., 1998; Warren et al., 1970) whereas it decreases with increasing differential stress (Scholz, 1968). Moreover, Urbancic et al. (1992) investigated possible space-time correlations between *b* values and several estimates of stress release such as static stress drop, dynamic stress drop, and apparent stress founding that a decrease of the b-value best correlates with dynamic stress drop.

Following the approach proposed by Urbancic et al. (1992), we select a set of earthquakes enclosed in a sphere centered on each earthquake for which the static stress drop is available. The radius of the sphere is set to 6 km whereas the time spans 30 days before and after the origin time of the considered event. For those events having at least 100 proximal earthquakes we compute the *b*-value using the *b*-more-positive technique (Lippiello and Petrillo, 2024), the uncertainty by using the Shin and Bolt (1982) approach. We compute both the linear fitting on the whole dataset and, following by Urbancic et al. (1992), a linear fit on the data obtained by applying a moving average. This latter allows to filter out statistical noise – due to the uncertainty of stress drop estimates in our case –, highlights the physical trend, and yields a more stable and interpretable fit. The results are shown in Figure 10 indicating a slight positive correlation between the two parameters which, however, is not significative since the corresponding R-values are 0.0009 and 0.0113, respectively.

5.1 Physical interpretation of *b*-value and stress drop correlation in Hengill

Here, we would like to explain the observed non-negative correlation between the *b*-value and stress drop ($\Delta\sigma$) in the Hengill geothermal field. Indeed, negative values have been observed in several different tectonic settings. Our key hypothesis is that ductile, strongly rate-dependent deformation increases fracture energy G with slip velocity suppressing earthquake cascades; thus, increasing the *b*-value.

In ductile regimes, weakening mechanisms introduce a strong rate-dependence in the energy needed to promote fracturing (Cocco et al., 2023). We model this effect via a characteristic slip distance $D_c(v) = D_{c0}(v/v_0)^{\alpha}$, with $\alpha > 0$ (α is a dimensionless parameter quantifying the ductile effect) and v represents slip velocity (e.g., Nielsen et al., 2016). Such mechanisms are also observed in brittle regimes during large earthquakes, but they only play a negligible role in microseismicity. The fracture energy is found by integrating the weakening curve over slip *s*:

$$G(v) = \int_0^{\infty} (\tau(s) - \tau_{ss})\, ds \propto v^{\alpha} \qquad (6)$$

Where $\tau(s)$ is the shear stress and τ_{ss} is the steady state shear stress on fault. For a circular crack, the energy balance $\frac{(\Delta\sigma)^2}{\mu} r^3 \gtrsim G r^2$ implies that a minimum triggered asperity size exists corresponding to a radius $r_{\min} \propto \frac{\mu G}{(\Delta\sigma)^2} \propto v^{\alpha}$.

This makes dynamic propagation more difficult, as larger cascades are needed to trigger asperities with similar spatial extension.

We model a fault system as a set of asperities following a size distribution $n(r) \propto r^{-\delta}$, where $\delta \simeq 3$, representing fault structural heterogeneity (Cowie et al., 1995). By transforming the size distribution $n(r)$ into a moment distribution $n(M_0)$ using the relationship $M_0 \propto r^3$ (Udias et al., 2014), we obtain the Gutenberg-Richter power law exponent $\beta_{brittle} = \frac{\delta}{3} + \frac{2}{3} - 1 = \frac{\delta - 1}{3}$, which corresponds to a *b*-value $b_{\mathrm{brittle}} = \frac{\delta - 1}{2} \approx 1$.

The ductile, rate-dependent weakening suppresses the triggering of larger asperities, as their higher slip velocities face an increased fracture energy barrier according to Equation 6. We model this cascade-stopping effect with a triggering probability that decays with the asperity size: $P_{\text{cascade}}(r) \propto r^{-\gamma}$, where γ increases monotonically with α. Then, the distribution of sizes becomes $n(r) \propto r^{-(\delta+\gamma)}$ resulting in a b-value

$$b_{\text{ductile}} = b_{\text{brittle}} + \frac{\gamma}{2} \qquad (7)$$

Therefore, the presence of ductile components increases the *b*-value by suppressing large cascades. To connect this result with stress drops, we refine the triggering probability to be $P_{\text{cascade}} \propto (\Delta\sigma)^m r^{-\gamma}$. This formula captures the idea that earthquakes associated with higher stress drops statistically produce larger stress perturbations nearby, hence increasing seismic productivity. In brittle regimes (where α is smaller or negligible), higher Δσ efficiently promotes cascading, fostering larger events and lowering the *b*-value, so that

$$\frac{\partial b_{\text{brittle}}}{\partial \Delta\sigma} \propto -m_b < 0 \quad (8)$$

Where m_b corresponds to the exponent *m* for brittle regimes. In ductile regimes, higher Δσ also increases the slip velocity v, thereby increasing the fracture energy $G(v) \propto (\Delta\sigma)^{\alpha}$ that must be overcome. This suppresses cascade efficiency, leading to $m_d \approx 0$ (*m* for ductile regimes) or potentially even negative. Consequently,

$$\frac{\partial b_{\text{ductile}}}{\partial \Delta\sigma} \propto -m_d \gtrsim 0 \quad (9)$$

In summary, above the brittle-ductile transition, high stress drops facilitate cascades, producing larger events and a lower *b*-value. In ductile settings like in Hengill, high stress drops are associated with intense rate-dependent dissipation, which reduces cascade propagation. This suppression of major earthquakes results in a higher *b*-value, potentially explaining null or positive correlations between the *b*-value and stress drops.

6 Conclusions

We have analyzed 8691 events with magnitude in the range (−0.8, 4.6) recorded at Hengill geothermal field in Iceland between 2018 and 2021to infer kinematic and dynamic seismic source properties. We have implemented both the individual earthquake approach and the EGFs approach, which allows to reduce the possible trade-off between seismic source parameters, such as corner frequency and anelastic attenuation.

We can summarize the main results and implications of our results as follows:

- the scaling between seismic moment and corner frequency slightly deviates from the self-similar predicted trend.
- the mean static stress drop value of 6.5 ± 13.2 MPa is higher than the value of 4 MPa proposed for global tectonic earthquakes (Allmann and Shearer, 2009).
- the observed depth dependence of the static stress drop suggests induced and tectonic earthquakes may have different stress drop. This is in contrast with the results provided by Huang et al. (2017) obtained analyzing induced and tectonic events record in Central United States and those obtained by Convertito and De Matteis (2025) from the analysis of the St. Gallen, Switzerland, induced earthquakes.
- the ratio $\Delta\sigma/S$ varies systematically with depth. Shallow earthquakes in Hengill appear to be strongly influenced by fluid-assisted weakening, whereas deeper events are more stress-controlled.
- low radiation efficiency indicates a positive dynamic overshoot, that is, the seismically radiated energy is only a small fraction of the total available energy.
- in geothermal fields like Hengill, the correlation between *b*-value and stress drop reflects the contributing and sometimes dominant role of ductile processes. Higher stress drops require faster slip velocity, which in turn increases the fracture energy. This enhanced energy dissipation suppresses the rupture cascade necessary to create large earthquakes, resulting in a higher proportion of small events (higher *b*-value) despite the increased stress drop. Thus, a null or slightly positive *b*-value *vs.* stress drop correlation from a high dissipation in these specific geological settings.

Acknowledgments

The publication was produced with the co-financing of the European Union - Next Generation EU. This publication has been supported by the project titled D.I.R.E.C.T.I.O.N.S. - Deep learning aIded foReshock deteCTIOn Of iNduced mainShocks, project code: P20220KB4F, CUP: E53D23032910001, PRIN 2022 - Piano Nazionale di Ripresa e Resilienza (PNRR), Mission 4 “Istruzione e Ricerca” - Componente C2 Investimento 1.1, “Fondo per il Programma Nazionale di Ricerca e Progetti di Rilevante Interesse Nazionale (PRIN)”. This publication was partially supported by the project Nonlinear models for magma transport and volcanoes generation- project code: P20222B5P9, PRIN 2022 PNRR.

Open Research

The figures were created by using Generic Mapping tools (GMT) by Wessel et al. (2019) and Matplotlib by Hunter (2007). The waveforms used in this paper are available at (Convertito et al., 2025). Waveform data for each event are available via Swiss Seismological Service (SED) webservice (http://eida-federator.ethz.ch) and the GFZ Helmholtz Centre for Geosciences (http://geofon.gfz-potsdam.de).

References

Abercrombie, R. E. (1995). Earthquake source scaling relationships from −1 to 5 ML using seismograms recorded at 2.5-km depth. *J. Geophys. Res.*, 100(B12), 24, 015–24, 036, doi:10.1029/95JB02397.

Abercrombie, R.E. (2014). Stress drops of repeating earthquakes on the San Andreas Fault at Parkfield. *Geophys. Res. Lett.*, 41, 8784–8791, doi:10.1002/2014GL062079.

Abercrombie, R.E. (2015). Investigating uncertainties in empirical Green's function analysis of earthquake source parameters. *J. Geophys. Res.*: *Solid Earth*, 120(6), 4263-4277.

Abercrombie, R.E., & Leary, P. (1993). Source Parameters of Small Earthquakes Recorded at 2.5 km Depth, Cajon Pass, Southern California: Implications for Earthquake Scaling. *Geophys. Res. Lett.*, 20, 1511–1514.

Abercrombie, R.E., & Rice, J. R. (2005). Can observations of earthquake scaling constrain slip weakening?. *Geophys. J. Int.*, 162(2), 406-424.

Allmann, B.P., & Shearer, P.M. (2009). Global variations of stress drop for moderate to large earthquakes. *J. Geophys. Res.*, 114, B01310, doi:10.1029/2008JB005821.

Amoroso, O., Napolitano F., Hersir G.P., Agustsdottir T., Convertito V., De Matteis R., Gunnarsdóttir S.H., Hjörleifsdóttir V. & Capuano P. (2022). 3D seismic imaging of the Nesjavellir geothermal field, SW-Iceland. *Front. Earth Sci.*, 10:994280. doi: 10.3389/feart.2022.994280.

Beeler, N. M., Wong, T. F., & Hickman, S. H. (2003). On the expected relationships among apparent stress, static stress drop, effective shear fracture energy, and efficiency. *Bull. Seismol. Soc. Am.*, 93(3), 1381-1389.

Beeler, N. M. (2006). Inferring earthquake source properties from laboratory observations and the scope of lab contributions to source physics, vol. 170, 99–119 (American Geophysical Union (AGU), 2006).

Ben-Menahem, A., & Singh, S.J. (1981). Seismic Waves and Sources, 1108 p, Springer-Verlag, New York.

Boatwright, J. (1980). A spectral theory for circular seismic sources; simple estimated of source dimension, dynamic stress drop, and radiated seismic energy. *Bull. Seismol. Soc. Am.*, 70(1), 1–27.

Boatwright, J., Choy, & Seekins, L. C. (2002). Regional Estimates of Radiated Seismic Energy. *Bull. Seismol. Soc. Am.*, 92 (4): 1241–1255. doi: https://doi.org/10.1785/0120000932.

Boore, D. M., & Boatwright, J. (1984). Average body-wave radiation coefficients. *Bull. Seism. Soc. Am.*, 74, 2035-2039.

Brune, J. N. (1970). Tectonic stress and the spectra of seismic shear waves from earthquakes. *J. Geophys. Res.*, 75(26), 4997–5009, doi:10.1029/JB075i026p04997.

Cocco, M., Aretusini, S., Cornelio, C., Nielsen, S.B., Spagnuolo, E., Tinti, E., Di Toro, G. (2023). Fracture energy and breakdown work during earthquakes. *Ann. Rev. Earth Planet. Sci.* 51, 217–252.

Cowie, P.A., Sornette, D., & Vanneste, C. (1995). Multifractal scaling properties of a growing fault population. *Geophys. J. Intern.* 122, 457–469.

Convertito, V., Maercklin, N., Sharma, N. & Zollo, A. (2012). From Induced Seismicity to Direct Time-Dependent Seismic Hazard. *Bull. Seism. Soc. Am.*, 102, 2563–2573. doi: https://doi.org/10.1785/0120120036.

Convertito V., Ebrahimian, H., Amoroso, O., Jalayer, F., De Matteis, R., & Capuano, P. (2021). Time-Dependent Seismic Hazard Analysis for Induced Seismicity: The Case of St. Gallen (Switzerland), Geothermal Field. *Energies.* 14, 2747. https://doi.org/10.3390/en14102747.

Convertito, V., & De Matteis, R. (2025). Kinematic and dynamic source parameters of induced earthquakes at St. Gallen geothermal field, Switzerland. *J. Geophys. Res.*: Solid Earth, 130, e2024JB030072. https://doi.org/10.1029/2024JB030072.

Convertito, V., Godano, C., Petrillo, G. et al. Insights from b value analysis of Campi Flegrei unrests. *Sci. Rep.*, 15, 14974 (2025). https://doi.org/10.1038/s41598-025-98240-4.

Convertito, V., Gammaldi, S., Zaccagnino, D., Godano, C., & De Matteis, R. (2025), Rheological control on earthquake source kinematics and dynamics at the Hengill geothermal field [Datasets]. (http://eida-federator.ethz.ch) and (http://geofon.gfz-potsdam.de).

Decriem, J., et al. (2010). The 2008 May 29 earthquake doublet in SW Iceland, *Geophys. J. Int.*, 181, 1128 1146.

De Matteis, R., Massa, B., Adinolfi, G. M., Amoroso, O., Terakawa, T., & Convertito,V. (2024). Pore fluid pressure in St. Gallen geothermal field (Switzerland) based on earthquake focal mechanisms. *Geophys. Res. Lett.*, 51, e2023GL105127. https://doi.org/10.1029/2023GL105127.

Douglas, J., Edwards, B., Cabrera, B.M., Convertito, V., Tramelli, A., Kraaijpoel, D., Maercklin, N., Sharma, N., & Troise, C. (2013). Predicting ground motion from induced earthquakes in geothermal areas. *Bull. Seismic. Soc. Am.*, 103, 1875–1897.

Gammaldi, S., Cabrera-Pérez, I., Koulakov, I., D'Auria, L., Barberi, G., García-Hernández, R., et al. (2025). Seismic tomography of a newborn volcano. *Geophys. Res. Lett.*, 52, e2025GL114932.

Goertz-Allmann, B. P., and S. Wiemer (2013), Geomechanical modeling of induced seismicity source parameters and implications for seismic hazard assessment. *Geophysics*, 78(1), KS25–KS39, doi:10.1190/GEO2012-0102.1.

Grigoli, F., Clinton, J. F., Diehl, T., Kaestli, P., Scarabello, L., Agustsdottir, T., et al. (2022). Monitoring microseismicity of the Hengill geothermal field in Iceland. *Sci. Data*, 9(1), 220.

Hensch, M., Björn Lund, Thóra Árnadóttir, Bryndís Brandsdóttir (2016). Temporal stress changes associated with the 2008 May 29 MW 6 earthquake doublet in the western South Iceland Seismic Zone. *Geophys. J. Int.*, 204, 1, 544–554.

Huang, Y., Ellsworth, W.L., & Beroza, G.C. (2017). Stress drops of induced and tectonic earthquakes in the central United States are indistinguishable. *Sci. Adv.* 3, e1700772.

Hunter, J.D. (2007). Matplotlib: A 2D Graphics Environment. *Computing in Science & Engineering*, vol. 9, no. 3, pp. 90-95. doi: 10.1109/MCSE.2007.55.

Husseini, M. I., & Randall, M. (1976). Rupture velocity and radiation efficiency. *Bull. Seismol. Soc. Am.*, 66, 1173–1187.

Ide, S., & Beroza, G. C. (2001). Does apparent stress vary with earthquake size?. *Geophys. Res. Lett.*, 28, 3349–3352.

Ide, S., Beroza, G.C., Prejean, S.G., & Ellworth, W.L. (2003). Apparent break in earthquake scaling due to path and site effects on deep borehole recordings. *J. Geophys. Res.*, 108(B5), 2271, doi:10.1029/2001JB001617.

Kanamori, H., & Heaton, T. H. (2000). Microscopic and macroscopic physics of earthquakes, in GeoComplexity and the Physics of Earthquakes. *Geophysical Monograph*, vol. 120, pp. 147–163, AGU, Washington, D. C.

Kanamori, H., & Rivera, L. (2004). Static and Dynamic Scaling Relations for Earthquakes and Their Implications for Rupture Speed and Stress Drop. *Bull. Seismol. Soc. Am.*, 94, 314–319.

Kwiatek, G., K. Plenkers, and G. Dresen (2011), Source parameters of picoseismicity recorded at Mponeng Deep Gold Mine, South Africa: Implications for scaling relations. *Bull. Seismol. Soc. Am.*, 101(6), 2592–2608, doi:10.1785/0120110094.

Lippiello, E., & Petrillo, G. (2024). b-more-incomplete and b-more-positive: Insights on a robust estimator of magnitude distribution. *J. Geophys. Res.: Solid Earth*, 129, e2023JB027849. https://doi.org/10.1029/2023JB027849.

McGarr, A. (1999). On relating apparent stress to the stress causing earthquake fault slip. *J. Geophys. Res.*, 104, 3003–3011.

Michelini, A., Cianetti, S., Gaviano, S., Giunchi, C., Jozinović, D., & Lauciani, V. (2021). INSTANCE – the Italian seismic dataset for machine learning. *Earth Syst. Sci. Data*, 13, 5509–5544. https://doi.org/10.5194/essd-13-5509-2021.

Mogi, K. (1962). Study of the elastic shocks caused by the fracture of heterogeneous materials and its relation to earthquake phenomena. *Bull. Earthq. Res. Inst.*, Tokyo Univ. 40, 125–173.

Mousavi, S. M., Sheng, Y., Zhu, W., & Beroza, G. C. (2019). Stanford Earthquake Dataset (STEAD): A global dataset of seismic signals for AI. IEEE Access, 7, 179464–179476. https://doi.org/10.1109/ACCESS.2019.2947848.

Napolitano, F., De Siena, L., Amoroso, O., Ágústsdóttir, T., Benediktsdóttir, Á., Palo, M., et al. (2025). Scattering and absorption imaging of the Hengill high-temperature geothermal area, Southwest Iceland. *J. Geophys. Res.*: Solid Earth, 130(5), e2024JB030731.

Nielsen, S., Spagnuolo, E., Violay, M., Smith, S., Di Toro, G., Bistacchi, A. G. (2016). Fracture energy, friction and dissipation in earthquakes. *J. Seismol.* 20, 1187–1205.

Obermann, A., Wu S.-M., Ágústsdóttir T., Duran A., Diehl T., Sánchez-Pastor P., Kristjansdóttir S., Hjörleifsdóttir V., Wiemer S. & Hersir G.P. (2022). Seismicity and 3-D body-wave velocity models across the Hengill geothermal area, SW Iceland. *Front. Earth Sci.* 10:969836. doi: 10.3389/feart.2022.969836.

Prejean, S.G., & Ellsworth, W. L. (2001). Observations of Earthquake Source Parameters at 2 km Depth in the Long Valley Caldera, Eastern California. *Bull. Seism. Soc. Am.*, 91 (2): 165–177. doi: https://doi.org/10.1785/0120000079.

Prieto, G. A., Parker, R. L., Vernon, F. L., Shearer, P. M., & Thomson, D. J. (2006). Uncertainties in earthquake source spectrum estimation using empirical Green functions, in Earthquakes: Radiated Energy and the Physics of Faulting, pp. 69–74, Washington, D. C.

Prieto, G.A., Parker, R.L., Thomson, D.J., Vernon, F.L., & Graham, R.L. (2007). Reducing the bias of multitaper spectrum estimates. *Geophys. J. Int.*, 171, 1269–1281.

Shi, Y., and Bruce A. Bolt (1982). The standard error of the magnitude-frequency b value. *Bull. Seism. Soc. Am.,* 72 (5): 1677–1687. doi: https://doi.org/10.1785/BSSA0720051677.

Scholz, C., (1968), The frequency-magnitude relation of microfracturing inrock and its relation to earthquakes. *Bull. Seismol. Soc. Am.*, 58,399–415.

Toksoz, M.N., Johnston, A.H., and Timur, A. (1979), Attenuation of seismic waves in dry and saturated rocks. I. Laboratory measurements. *Geophysics*, 44, 681-690.

Udıas, A., Madariaga, R., Buforn, E. (2014), Source mechanisms of earthquakes: Theory and practice. Cambridge University Press.

Urbancic, T.I., C.I. Trifu, J.M. Long, and R.P. Toung, (1992). Space-time correlations of b values with stress release. *Pure Appl. Geophys.*,1 39, 449462.

Wang, J., Xiao, Z., Liu, C., Zhao, D., & Yao, Z. (2019). Deep learning for picking seismic arrival times. *J. Geophys. Res.*: Solid Earth, 124, 6612–6624. https://doi.org/10.1029/2019JB017536.

Warren, N. W. & Latham, G. V. (1970). An experimental study of thermally induced microfracturing and its relation to volcanic seismicity. *J. Geophys. Res.*, 75, 4455–4464.

Wessel, P., Luis, J. F., Uieda, L., Scharroo, R., Wobbe, F., Smith, W. H.F., & Tian, D. (2019). The Generic Mapping Tools version 6. *Geochemistry, Geophysics, Geosystems*, 20, 5556–5564.https://doi.org/10.1029/2019GC008515.

Wiemer, S., McNutt, S. R. & Wyss, M. (1998). Temporal and three-dimensional spatial analyses of the frequency–magnitude distribution near Long Valley Caldera, California. *Geophys. J. Int.*, 134,409–421.

Wyss, M. (1979). Observation and interpretation of tectonic strain release mechanisms, PhD thesis, Calif. Inst. of Technol., Pasadena.

Wu, S.-M., Sánchez-Pastor, P., Ágústsdóttir, T., Hersir, G.P., Mordret, A., Hjörleifsdóttir, V., & Obermann, A. (2024). Crustal characterization of the Hengill geothermal fields: Insights from isotropic and anisotropic seismic noise imaging using a 500-node array. *J. Geophys. Res.*: Solid Earth, 129, e2024JB028915. https://doi.org/10.1029/2024JB028915.

Zhao M, Xiao ZW, Chen S and Fang LH (2023). DiTing: A large-scale Chinese seismic benchmark dataset for artificial intelligence in seismology. *Earthq Sci* 36(2): 84–94. https://doi.org/10.1016/j.eqs.2022.01.022.

Zollo, A., Orefice, A., & Convertito, V. (2014). Source parameter scaling and radiation efficiency of microearthquakes along the Irpinia fault zone in southern Apennines, Italy. *J. Geophys. Res.*: *Solid Earth*, 119(4), 3256-3275.